RSC Advances

ROYAL SOCIETY OF CHEMISTRY

www.rsc.org/advances

RSC Advances

RSCPublishing

COMMUNICATION

Synthesis and fast-response photodetector of hydrothermally grown ZnO nanorods through the use of graphene oxide/ZnO seed layer†

Cite this: DOI: 10.1039/xoxxoooooox

Received ooth January 2012,
Accepted ooth January 2012

DOI: 10.1039/xoxxoooooox

www.rsc.org/MaterialsC

Giwoong Nam and Jae-Young Leem*

We used a hydrothermal method combined with a graphene oxide (GO)/ZnO seed layer to fabricate ZnO nanorod based fast-response UV detector. The introduction of GO film decreases excitonic photoluminescence intensity, which indicates the transfer of electrons from ZnO nanorods to the surface of the GO film (quenching).

One-dimensional (1D) nanostructures, including nanorods, nanowires, and nanotubes, have aroused considerable research interest in numerous areas of nanoscience and nanotechnology. There are two reasons for this interest: first, 1D nanostructures have unusual and unique physical properties, such as quantum-mechanical confinement effects (QCEs);[1] second, they have a high surface-to-volume ratio, making them important for the development of new devices and sensors.[2] It is believed that QCEs play a crucial role in improving the optical properties of materials.[3] Zinc oxide (ZnO) exhibits a direct bandgap of 3.37 eV, a high exciton binding energy of 60 meV (considerably larger than the 25 meV exciton binding energy of gallium nitride), and a favorable thermal energy of ~26 meV at room temperature (RT), which act together to ensure efficient exciton emission under ambient conditions. 1D ZnO nanomaterials could potentially be used in a broad range of high-performance applications could potentially use, such as UV lasers, photodetectors, field-effect transistors, solar cells, chemical sensors, superhydrophobic surfaces, and nanogenerators.[4]

Many approaches, such as vapor-phase and solution-phase synthesis, electrospinning, and templating, have been developed for creating 1D nanomaterials.[5] Among these methods, vapor-phase and solution-phase synthesis are the most dominant approaches. Compared to vapor-phase synthesis, solution-phase techniques have many advantages, such as scalability, low cost, and ease of handling. More importantly, solution synthesis methods allow for a greater choice of substrates, including both inorganic and organic substrates, since solution-phase reactions occur at relatively low temperatures (25–200 °C) compared to those in the vapor-phase (> 450 °C). Accordingly, the synthesis of high-quality 1D ZnO nanostructures grown by solution-phase reactions is important for both basic fundamental research and industrial applications. In most of the papers, however, there are problems such as low optical and photoresponse properties of ZnO nanorods.[6]

The ZnO nanorods or films on graphene oxide (GO) or graphene has been recently reported and GO is fabricated by chemical vapor deposition.[7] However, the oxidation and reduction of graphite is one of the most effective methods in mass production of GO for industrial applications. In this study, we fabricated GO from graphite according to the modified Hommers and Offeman method[8] and used a hydrothermal method combined with a GO/ZnO seed layer to fabricate ZnO nanorod based fast-response UV detector. ZnO nanorods with rapid UV response can be fabricated by using a GO/ZnO seed layer, compared with a ZnO seed layer. The effects of the GO/ZnO seed layer on the structural, photoresponse, and optical properties of the ZnO nanorods were investigated. In particular, the optical properties of the ZnO nanorods were investigated by temperature-dependent photoluminescence (PL), which is one of the most widely used experimental methods for studying the optical properties of semiconductors.

Two different samples were prepared for a comparative study as shown in Fig. S1 (ESI†). For samples 1 and 2, solution 1 was spin-coated onto a p-Si substrate at 2000 rpm for 20 s, and the ZnO films were then dried at 200 °C for 10 min in an oven. These spin-coating and drying procedures were repeated three times. Additionally, sample 2 was spin-coated with GO film on the ZnO film at 2000 rpm for 20 s, and the GO/ZnO films were dried at 200 °C for 10 min in an oven. Both samples were annealed in a furnace at 600 ºC for 1 h. The ZnO nanorods were then hydrothermally grown on samples 1 and 2. Samples 1 and 2 were transferred to a Teflon-lined autoclave containing an aqueous solution of 0.02 M zinc nitrate hexahydrate ($Zn(NO_3)_2 \cdot 6H_2O$), hexamethylenetetramine ($(CH_2)_6N_4$, HMT), and sodium hydroxide (NaOH). The nanorods were hydrothermally grown in the autoclave at 80 °C for 6 h (further experimental detail can be found in supplementary methods, ESI†).

Raman spectroscopy is a widely used technique to chracterize graphite materials, especially to determine ordered and disordered crystal structures of graphene.[9] The Raman spectrum of the GO film (Fig. 1a) displays two prominent peaks at 1350 and 1595 cm^{-1}, which correspond to the D and G band, respectively. The D band at 1350 cm^{-1} is related to the vibration of sp^3 carbon atoms in defects and disordered regions, and the G band is associated with the vibration of sp^2 carbon atoms in a graphitic 2D hexagonal lattice.[10] The weak and broad 2D peak at 2660 cm^{-1} is another indication of disorder due to an out-of-plane vibrational mode, and the interaction

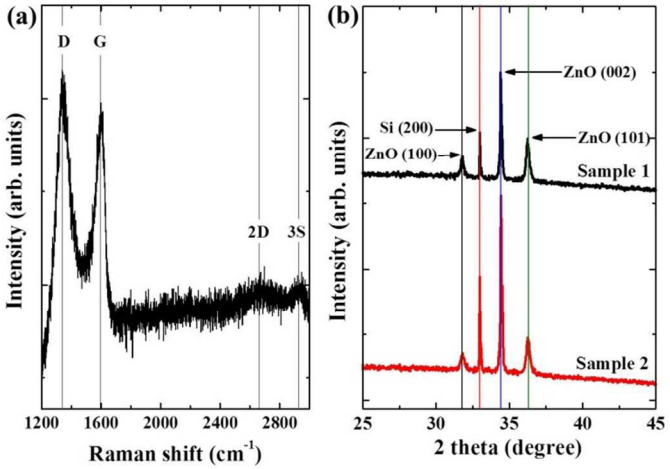

Fig. 1 (a) Raman spectrum of GO film and (b) XRD spectra of samples 1 and 2.

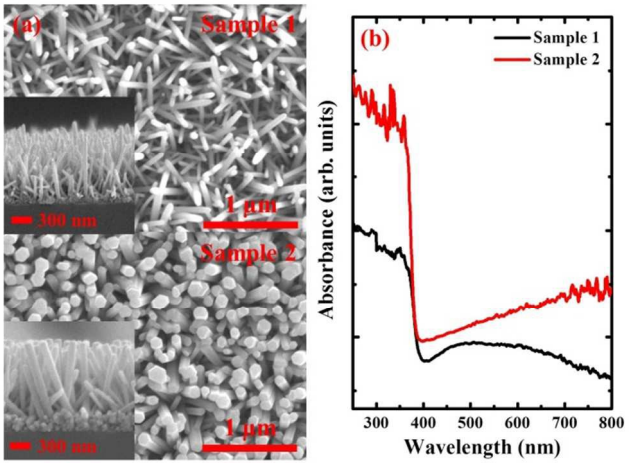

Fig. 2 (a) SEM images and (b) UV-vis absorption spectra of the samples 1 and 2.

between D and G peaks also give rise to an S3 peak near 2925 cm^{-1}.[10c,10d] Fig. 1b shows X-ray diffraction patterns of samples 1 and 2. Three ZnO diffraction peaks were observed at 31.78°, 34.42°, and 36.25°, which correspond to the ZnO (100), (002), and (101) planes, respectively. No traces of graphite diffraction peaks were detected, indicating that the surface of the GO was fully covered with ZnO nanorods for all samples.[11] Two samples exhibited a strong (002) peak, indicating that the c-axis orientation of the ZnO grains was perpendicular to the substrate. It was also observed that the intensity of the (002) peak in sample 2 was larger than that in sample 1.

Fig. 2a shows the SEM images of samples 1 and 2. The morphology of ZnO nanorods were found to be related to the addition of GO. The diameter of the ZnO nanorods were measured to be 50 nm on sample 1 and 80 nm on sample 2. In sample 2, dense ZnO nanorods with hexagonal wurtzite structures were observed to be uniformly distributed on GO/ZnO films. However, in sample 1, the ZnO nanorods grown on ZnO films had a disordered orientation. In our experiment, the GO/ZnO film on Si substrate was immersed in aqueous solution of $Zn(NO_3)_2 \cdot 6H_2O$ acting as Zn source, HMT as OH^- source, and NaOH to get an alkaline solution (pH 12). Reactions (1) and (2) present the formation of OH^- from the HMT molecule. The first reaction decomposes HMT into HCHO and NH_3 and, afterward, the second reaction involves NH_3 and H_2O to provide OH^- ions upon slow heating. The OH^- ions react with Zn^{2+} from $Zn(NO)_3$ at elevated temperature to generate $Zn(OH)_2$ and, subsequently, the dehydration of $Zn(OH)_2$ forms ZnO nuclei on top of the GO or ZnO film, as expressed by the reactions (3) and (4).

$$(CH_2)_6N_4 + 6H_2O \rightarrow 6HCHO + 4NH_3 \quad (1)$$

$$NH_3 + H_2O \rightarrow NH_4^+ + OH^- \quad (2)$$

$$Zn^{2+} + 2OH^- \rightarrow Zn(OH)_2 \quad (3)$$

$$2Zn(OH)_2 \rightarrow ZnO + H_2O + 2OH^- \quad (4)$$

GO consists of graphene layers with epoxy and hydroxyl groups attached to the basal planes, and carbonyl and carboxyl groups at the edge planes.[12] The surface of the GO film tends to absorb positively charged metal ions (Zn^{2+}) and salts.[13] The absorbed Zn^{2+} ions provide spherical ZnO nuclei by the reaction with OH^- ions. The UV-visible absorption spectra of samples 1 and 2 are shown in Fig. 2b. Both samples displayed an absorption edge at 365 nm, which was assigned to the intrinsic absorption of ZnO nanocrystals. It was observed that the absorbance of sample 2 was larger than that of sample 1 througout the spectrum. The presence of GO increased the light absorption intensity, which may be due to the increase of surface electric charge of the oxides in GO/ZnO film and the modification of the fundamental process of electron-hole pair formation during irradiation.[14] The insets of Fig. 2(a) show the cross-section SEM images of samples 1 and 2. The ZnO nanorods in sample 2 exhibited a hexagonal shape compared with those in sample 1, demonstrating the high quality of ZnO crystals and their c-axis growth along the (002) plane, which is consistent with the XRD measurement.

Raman scattering was performed to investigate the vibrational properties of two samples. The space group of the hexagonal wurtzite ZnO belongs to c_{6v}^4 ($P6_3mc$). According to the group theory, single-crystalline ZnO has eight sets of optical phonon modes at Γ point of the Brillouin zone. There are $A_1 + E_1 + 2E_2$ (Raman active), $2B_1$ (Raman silent), and $A_1 + E_1$ (infrared active) modes. Moreover, the A_1 and E_1 modes split into LO and TO components. The Raman spectra of samples 1 and 2 are shown in Fig. S2. The peaks at 300, 520, and 616 cm^{-1} were due to scattering from the Si substrate. The band at 435 and 437 cm^{-1} in samples 1 and 2, respectively, is attributed to ZnO nonpolar optical phonons $E_2(H)$ mode of hexagonal ZnO. The stress induced in crystal would obviously affect the $E_2(H)$ phonon frequency in the hexagonal wurtzite structure crystals.[15] The upshift of $E_2(H)$ mode is correlated with the presence of compressive stress, while the downshift of that is related with tensile stress. The $E_2(H)$ mode in bulk ZnO crystal occurs at 437 cm^{-1}.[15] The sample 2 was the same position as the bulk ZnO crystal, which indicates that the sample 2 is free of stress. However, the $E_2(H)$ frequency in sample 1 was 2 cm^{-1} lower than that in the bulk ZnO crystal, which implies that the sample 1 is under tensile stress. We proposed that the introduction of GO film into ZnO nanorods could decrease the stress of ZnO nanorods. The peaks at 97, 379, and 408 cm^{-1} were attributed to $E_2(L)$, $A_1(TO)$, and $E_1(TO)$ of ZnO, respectively. The peak at 330 and 665 cm^{-1} were assigned to multiple-phonon scattering processes. In sample 1, the peak at 230 cm^{-1} was exhibited, which could be related to defect-induced modes. As shown in the inset of Fig. S2, no Raman peaks related to GO or graphite were detected because the surface of the GO was fully covered with ZnO nanorods in two samples, which is consistent with the XRD results.

PL measurement was utilized to detect the movement of electrons or energy transfer between the ZnO nanorods and GO film. Fig. 3a shows the PL spectra of both samples at 300 K. A sharp UV emission at 3.286 eV and a broader green emission at 2.152 eV were recorded in both samples, which were attributed to free exciton (FX) emission from the wide band gap of ZnO and the recombination of electrons in single occupied oxygen vacancies in ZnO, respectively.[16] The introduction of GO film decreased excitonic PL intensity, indicating the transfer of electrons from the ZnO nanorods to the surface of GO film due to quenching.[17] Therefore, the

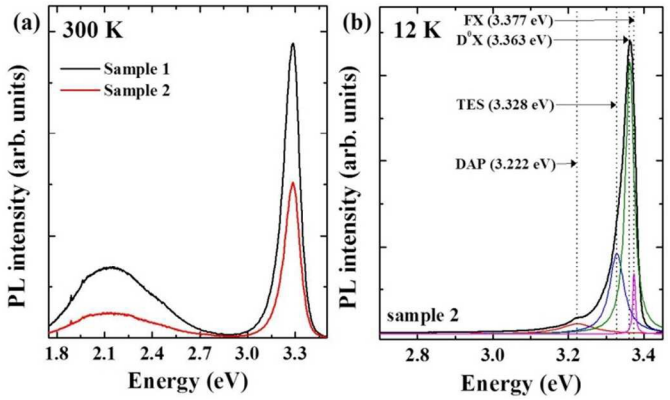

Fig. 3 (a) PL spectra of the samples 1 and 2 at 300 K, and (b) that of the sample 2 at 12 K

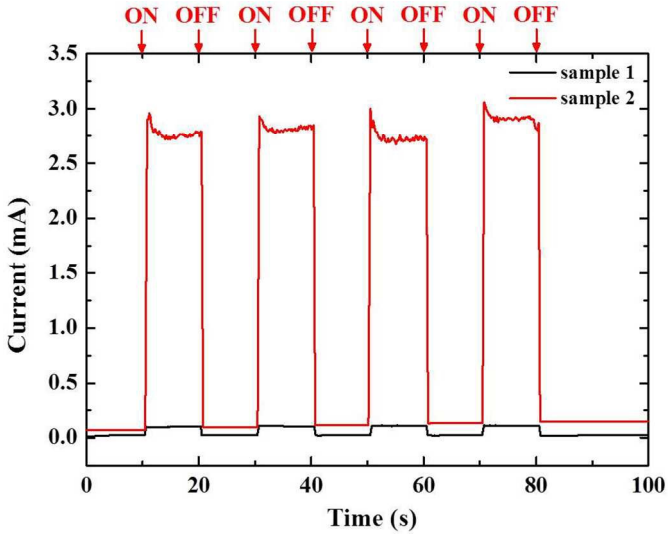

Fig. 4 Time-resolved photocurrent spectra at 5 V bias in response to the on/off switch of UV illumination (λ = 365 nm) for the two samples.

introduction of GO film into ZnO nanorods plays an important role in the photocatalytic performance of ZnO nanorods/GO film. Fig. 3b shows the PL spectrum of sample 2 measured at 12 K. Four distinct PL peaks appeared at 3.377, 3.363, 3.328, and 3.222 eV, which were attributed to the emission of FXs, neutral donor-bound excitons (D^0Xs), two-electron satellites (TESs), and donor-acceptor pairs (DAPs) transitions, respectively.[18]

In general, a TES is another characteristic of the D^0X transition in the spectral region of 3.32–3.34 eV.[18a] Bound excitons are extrinsic transitions related to dopants or defects, which usually create discrete electronic states in the band gap. In theory, excitons could be bound to neutral or charged donors and acceptors. The shallow neutral donor-bound exciton often dominates due to the presence of donors from unintentional impurities and/or shallow donor-like defects. During the recombination of a D^0X, the final state of the donor can be a 1s (the normal D^0_iX line) or a 2s/2p state (the TES_i line). The energy between the D^0_iX and its TES_i is the difference between the donor energies in the 1s and 2s/2p states. The donor excitation energy from the ground state to the first excited state is equal to 3/4 of the donor binding energy (E_D).[18a] According to the TES and D^0X peak positions, we calculated the E_D as 46.7 meV. The binding energy of a neutral donor's exciton was estimated as 14 meV based on the energy difference between the FX and D^0X emissions. This value is nearly identical to the activation energy for the thermal release of excitons from neutral donors. The E_D is estimated as 46.7 meV based on Haynes' empirical rule.[18a]

To study the origin of the UV emission in sample 2, PL spectra were measured at various temperatures from 12 to 300 K, as shown in Fig. S3a. The PL spectra contained various emission features that changed their intensities and positions based on temperature. The intensity of each peak decreased due to the thermally induced dissociation of electron-hole pairs with a rise in temperature. All of the peaks experienced redshift with increasing temperature. The redshift of FX and D^0X observed at a low temperature of 30 K arises due to thermal energy of localized carriers needed to overcome the localization potential at low temperature being insufficient; here these relax to lower-lying localized states prior to recombination. At high temperatures with sufficient thermal energy, the redshift is due to temperature induced bandgap shrinkage.[19] With increasing temperature, the DAP emission energy is slightly redshifted. The DAP emission energy is described as[18b]

$$h\nu = E_g - E_A - E_D + q^2/4\pi\varepsilon r, \quad (5)$$

where E_g is the band gap, E_A and E_D are the acceptor and donor binding energy, respectively, ε is the dielectric constant, and r is the donor-acceptor distance. With increasing temperature, carriers on DAP with small distance r are released into the band, and the line is shifted to the low-energy side. The D^0X emission was dominant at 12 K. However, the FX emission became dominant above 100 K, indicating that it was more probable for the bound excitons to ionize and eventually become FXs as the temperature increased. For the UV emission of a ZnO crystal, the dominance of the FX emission is usually attributed to the interband recombination of electrons and holes in form of excitons. Generally, due to the temperature-induced lattice dilatation and electron-lattice interaction, the interband emission peak energy follows the well-known Varshni formula:[19]

$$E_g(T) = E_g(0) - \alpha T^2/(\beta + T), \quad (6)$$

where T is the absolute temperature, $E_g(0)$ is the band-gap energy at $T = 0$ K, α and β are constants specific to ZnO, and β is proportional to the Debye temperature, θ_D. The α and β values obtained from fitting the FX were $\alpha = 0.52$ meV/K and $\beta = 218$ K, as shown in Fig. S3b.

The intensity of all PL peaks decreased with increasing temperature from 12 to 300 K, resulting from the thermally induced dissociation of electron-hole pairs as described by:[20]

$$I = I_0/[1 + C\exp(-\Delta E_A/k_B T)], \quad (7)$$

where I_0 is the emission intensity at $T = 0$ K, C is a constant, k_B is Boltzmann's constant, and ΔE_A is the activation energy for thermal quenching in Equation 7. The advantage of a large exciton binding energy for some device applications is clearly apparent. Indeed, the PL intensity increased nearly exponentially with the activation (binding or localization) energy at a given temperature. Fig. S4 shows the PL intensities of the D^0X and FX peaks as a function of inverse temperature for sample 2. The curves in Fig. S4 represent the best-fit results according to Equation 7. The activation energy was 14 meV for the D^0X peaks and 57 meV for the FX peaks. These activation energies accurately reflect the properties of the PL spectrum of sample 2 shown in Fig. 3b. Namely, the D^0X peaks at T < 100 K originate from the recombination of donor-bound excitons with a localization energy of 14 meV, a value identical to the localization energy in Fig. 3b; the FX peaks at T > 100 K originate from the recombination of free excitons with a binding energy of 57 meV, a value nearly identical to the exciton binding energy of ZnO (60 meV).[21]

Fig. 4 shows the photoresponse characteristics of three samples, which were measured at a bias voltage of 5 V under 365 nm UV illumination (20 mW/cm^2). As soon as the UV light is switched on, a considerable increase in current is observed, which is due to photogenerated carriers. The dark currents/photocurrents of samples

1 and 2 were 0.02/0.1 mA and 0.07/2.7 mA, respectively. When the holes combine with the absorbed oxygen atoms, the thickness of the depletion layer near the ZnO surface is decreased, which exhibits the exponential raise. When the UV light is switched off, the current follows a second order exponential decay. The photocurrent in sample 2 was larger than that in sample 1, because of the transfer of electrons from the ZnO nanorods to the surface of GO film, which is consistent with the absorbance and PL spectra. The result indicates that UV sensor of the sample 2 has the best UV photoresponse properties.

In summary, we used a hydrothermal method combined with a GO/ZnO seed layer to fabricate ZnO nanorod based fast-response UV detector. In XRD spectra, three ZnO diffraction peaks were observed at 31.78º, 34.42º, and 36.25º, which correspond to the ZnO (100), (002), and (101) planes, respectively. No traces of graphite diffraction peaks were detected, indicating that the surface of the GO was fully covered with ZnO nanorods for all samples. In PL spectrum analysis at 12 K, four distinct PL peaks appeared at 3.377, 3.363, 3.328, and 3.222 eV, which were attributed to the emission of FXs, D^0Xs, TESs, and DAPs transitions, respectively. The D^0X peaks at T < 100 K originate from the recombination of donor-bound excitons with a localization energy of 14 meV, a value identical to the localization energy; the FX peaks at T > 100 K originate from the recombination of free excitons with a binding energy of 57 meV, a value nearly identical to the exciton binding energy of ZnO (60 meV). The introduction of GO film into ZnO nanorods plays an important role in the photocatalytic performance of ZnO nanorods/GO film, and provides a new method to fabricate ZnO nanorods with rapid UV response.

This research was supported by Global PH.D Fellowship Program through the National Research Foundation of Korea (NRF) funded by the Ministry of Education (No. 2014H1A2A1018051).

Notes and references

Department of Nano Science & Engineering, Inje University, 197, Inje-ro, Gimhae-si, Gyeongsangnam-do, Republic of Korea
E-mail: jyleem@inje.ac.kr

† Electronic Supplementary Information (ESI) available: Experimental details and Temperature-dependent PL spectra of ZnO nanorods. See DOI: 10.1039/c000000x/

1 (*a*) D. Tsivion, M. Schvartzman, R. P. Biro, P. V. Huth and E. Joselevich, *Science*, 2005, **333**, 1003; (*b*) X. Liu, Q. Zhang, G. Xing, Q. Xiong and T. C. Sum, *J. Phys. Chem. C*, 2013, **117**, 10716; (*c*) H. Yin, Q. Wang, S. Geburt, S. Milz, B. Ruttens, G. Degutis, J. D'Haen, L. Shan, S. Punniyakoti, M. D'Olieslaeger, P. Wagner, C. Ronning and H.-G. Boyen, *Nanoscale*, 2013, **5**, 7046; (*d*) S. Li, C. Zhang, F. Li, W. Ji, P. Li, M. Ren, P. Wang and M. Yuan, *RSC Adv.*, 2014, **4**, 24399.

2 (*a*) R. Yu, C. Pan, J. Chen, G. Zhu and Z. L. Wang, *Adv. Funct. Mater.*, 2013, **23**, 5868; (*b*) S. N. Mohammad, *Nanotechnology*, 2013, **24**, 455201; (*c*) H. Nguyen, C. T. Quy, N. D. Hoa, N. T. Lam, N. V. Duy, V. V. Quang and N. V. Hieu, *Sens. Actuators B: Chem.*, 2014, **193**, 888.

3 (*a*) F. Qian, S. Gradecak, Y. Li, C.-Y. Wen and C. M. Lieber, *Nano Lett.*, 2005, **5**, 2287; (*b*) M. N. Makhonin, A. P. Foster, A. B. Krysa, P. W. Fry, D. G. Davies, T. Grange, T. Walther, M. S. Skolnick and L. R. Wilson, *Nano Lett.*, 2013, **13**, 861.

4 (*a*) M. H. Huang, *Science*, 2001, **292**, 1897; (*b*) Y. Lu, I. A. Dajani and R. J. Knize, *Electron. Lett.*, 2006, **42**, 1309; (*c*) D.-I. Suh, S.-Y. Lee, J.-H. Hyung, T.-H. Kim and S.-K. Lee, *J. Phys. Chem. C*, 2008, **112**, 1276; (*d*) J. Fan, Y. Hao, C. Munuera, M. Garcia-Hernandez, F. Guell, E. M. J. Johansson, G. Boschloo, A. Hagfeldt and A. Cabot, *J. Phys. Chem. C*, 2013, **117**, 16349; (*e*) D. Barreca, D. Bekermann, E. Commi, A. Devi, R. A. Fischer, A. Gasparotto, C. Maccato, C. Sada, G. Sberveglieri and E. Tondello, *CrystEngComm*, 2010, **12**, 3419; (*f*) P. Guo, Y. Zheng, M. Wen, C. Song, Y. Lin and L. Jiang, *Adv. Mater.*, 2012, **24**, 2642; (*g*) C.-Y. Chen, J.-H. Huang, J. Song, Y. Zhou, L. Lin, P.-C. Zhang, Y. Zhang, C.-P. Liu and Z. L. Wang, *ACS Nano*, 2011, **5**, 6707.

5 (*a*) S. C. Dhanabalan, J. P. Garcia, D. Calestani, F. Pattini, F. Bissoli, M. Villani, S. Rampino and A. Zappettini, *Cryst. Res. Technol.*, 2014, **49**, 558; (*b*) P. Rai, H.-M. Song, Y.-S. Kim, M.-K. Song, P.-R. Oh, J.-M. Yoon and Y.-T. Yu, *Mater. Lett.*, 2012, **68**, 90; (*c*) S. Bai, S. Chen, Y. Zhao, T. Guo, R. Luo, D. Li and A. Chen, *J. Mater. Chem. A*, 2014, **2**, 16697; (*d*) X. Wang, Y. Xu, H. Zhu, R. Liu, H. Wang and Q. Li, *CrystEngComm*, 2011, **13**, 2955.

6 (*a*) T. Ma, M. Guo, M. Zhang, Y. Zhang and X. Wang, *Nanotechnology*, 2007, **18**, 035605; (*b*) Y. Wang, X. Li, G. Lu, X. Quan and G. Chen, *J. Phys. Chem. C*, 2008, **112**, 7332.

7 (*a*) Y.-J. Kim, J.-H. Lee and G.-C. Yi, *Appl. Phys. Lett.*, 2009, **95**, 213101; (*b*) Q. Xu, Q. Cheng, J. Zhong, W. Cai, Z. Zhang, Z. Wu and F. Zhang, *Nanotechnology*, 2014, **25**, 055501; (*c*) R. K. Biroju, N. Tilak, G. Rajender, S. Dhara and P. K. Giri, *Nanotechnology*, 2015, **26**, 145601.

8 W. S. Hummers and R. E. Offeman, *J. Am. Chem. Soc.*, 1958, **80**, 1339.

9 G. Wang, X. Shen, J. Yao and J. Park, *Carbon*, 2009, **47**, 2049.

10 (*a*) X. Meng, D. Geng, J. Liu, M. N. Banis, Y. Zhang, R. Li and X. Sun, *J. Phys. Chem. C*, 2010, **114**, 18330; (*b*) D. Zhou and B.-H. Han, *Adv. Funct. Mater.*, 2010, **20**, 2717; (*c*) G. Eda and M. Chhowalla, *Adv. Mater.*, 2010, **22**, 2392; (*d*) T. V. Cuong, V. H. Pham, Q. T. Tran, S. H. Hahn, J. S. Chung, E. W. Shin and E. J. Kim, *Mater. Lett.*, 2010, **64**, 399.

11 Y.-L. Chen, Z.-A. Hu, Y.-Q. Chang, H.-W. Wang, Z.-Y. Zhang, Y.-Y. Yang and H.-Y. Wu, *J. Phys. Chem. C*, 2011, **115**, 2563.

12 G. Jiang, Z. Lin, C. Chen, L. Zhu, Q. Chang, N. Wang, W. Wei and H. Tang, *Carbon*, 2011, **49**, 2693.

13 A. Chrissanthopoulos, S. Baskoutas, N. Bouropoulos, V. Dracopoulos, D. Tasis and S. N. Yannopoulos, *Thin Solid Films*, 2007, **515**, 8524.

14 G. Williams and P. V. Kamat, *Langmuir*, 2009, **25**, 13869.

15 Y. Huang, M. Liu, Z. Li, Y. Zeng and S. Liu, *Mater. Sci. Eng. B*, 2003, **97**, 111.

16 S. Jiang, Z. Ren, S. Gong, S. Yin, Y. Yu, X. Li, G. Xu, G. Shen and G. Han, *Appl. Surf. Sci.*, 2014, **289**, 252.

17 (*a*) S. Ameen, M. S. Akhtar, H.-K. Seo and H. S. Shin, *Mater. Lett.*, 2013, **100**, 261; (*b*) F. Vietmeyer, B. Seger and P. V. Kamat, *Adv. Mater.*, 2007, **19**, 2935.

18 (*a*) Ü. Özgür, Y. I. Alivov, C. Liu, A. Teke, M. A. Reshchikov, S. Doğan, V. Avrutin, S.-J. Cho and H. Morkoç, *J. Appl. Phys.*, 2005, **98**, 041301; (*b*) L. Wu, Z. Gao, E. Zhang, H. Gao, H. Li and X. Zhang, *J. Lumin.*, 2010, **130**, 334.

19 Y. P. Varshni, *Physica*, 1967, **34**, 149.

20 F. Schuster, B. Laumer, R. R. Zamani, C. Mağen, J. R. Morante, J. Arbiol and M. Stutzmann, *ACS Nano*, 2014, **8**, 4376.

21 G. Nam, B. Kim, Y. Park, S. Park, J. Moon, D. Y. Kim, S.-O. Kim and J.-Y. Leem, *J. Mater. Chem. C*, 2014, **2**, 9918.